Applied Catalysis B: Environmental 99 (2010) 378–387

Contents lists available at ScienceDirect

Applied Catalysis B: Environmental

journal homepage: www.elsevier.com/locate/apcatb

Synthesis, structural characterization and evaluation of sol–gel-based NF-TiO_2 films with visible light-photoactivation for the removal of microcystin-LR☆

Miguel Pelaez[a], Polycarpos Falaras[b], Vlassis Likodimos[b], Athanassios G. Kontos[b], Armah A. de la Cruz[c], Kevin O'shea[d], Dionysios D. Dionysiou[a,*]

[a] Department of Civil and Environmental Engineering, University of Cincinnati, Cincinnati, OH 45221-0071, USA
[b] Institute of Physical Chemistry, NCSR Demokritos, 15310 Aghia Paraskevi, Attiki, Greece
[c] Office of Research and Development, U.S. Environmental Protection Agency, Cincinnati, OH 45268, USA
[d] Department of Chemistry and Biochemistry, Florida International University, University Park, Miami, FL 3319, USA

ARTICLE INFO

Article history:
Available online 15 June 2010

Keywords:
NF-TiO_2
Fluorosurfactant
Sol–gel method
Dip-coating
Nitrogen doped
Fluorine doped
Microcystin-LR
Photocatalysis
Visible light
TiO_2
EPR
Micro-Raman
Cyanotoxins
Water treatment
Sustainability

ABSTRACT

This study reports on the synthesis, characterization and environmental application of immobilized nitrogen and fluorine co-doped TiO_2 (NF-TiO_2) photocatalyst. A fluorosurfactant-based sol–gel approach was employed to enhance the physicochemical properties and photocatalytic activity of NF-TiO_2 under visible and UV light for the degradation of the hepatotoxin microcystin-LR (MC-LR). The films were characterized by XRD, environmental scanning electron microscope (ESEM), TEM, AFM, EPR, micro-Raman, X-ray photoelectron spectroscope (XPS), UV–vis spectroscopy and porosimeter analysis. The results revealed that by modifying the molar ratio of the fluorosurfactant, we could effectively control the physicochemical properties and obtain films with high BET surface area and porosity, small crystallite size and narrow pore size distribution. UV–vis spectroscopy showed an increase in the absorption capacity of NF-TiO_2 in the visible light range compared to reference films. The existence of interstitial nitrogen and substitutional fluorine in the titanium dioxide (TiO_2) lattice was determined by XPS. Comparative EPR measurements between the co-doped and reference samples identified distinct N spin species in NF-TiO_2, with a high sensitivity to visible light irradiation. The abundance of these paramagnetic centers verifies the formation of localized intra-gap states in TiO_2 and implies synergistic effects between fluorine and nitrogen dopants. Micro-Raman spectroscopy showed the growth of small amounts of brookite concomitantly with the major anatase TiO_2 phase, which could promote the system's photocatalytic activity through the formation of anatase/brookite heterojunctions. Analysis of the lower frequency E_g anatase Raman mode indicated the occurrence of size effects reflecting phonon confinement in the anatase nanocrystallites as well as deviations from stoichiometry due to structural defects in the co-doped sample. NF-TiO_2 films effectively degraded MC-LR under visible and UV light compared to reference film. Similar MC-LR degradation rates under visible light after three cycles revealed high mechanical stability and no irreversible changes of the film during photocatalysis. This process has the potential of providing environmentally benign routes for drinking water treatment with solar powered photocatalytic systems.

© 2010 Elsevier B.V. All rights reserved.

1. Introduction

Recent advances in the field of environmental nanotechnology show that this field can play a major role on global efforts towards finding sustainable solutions in response to the environmental crisis, including the need to secure sufficient and high quality drinking water. Moreover, the development of innovative processes using renewable sources of energy for environmental remediation associated with the current problems of water and air contamination has become a high priority towards an attempt to achieve global sustainability. Titanium dioxide (TiO_2) photocatalysis represents a promising technology for the treatment of emerging micropollutants found in air and water due to its high photocatalytic activity and 'green' characteristics. TiO_2 is relatively non-toxic, relatively inexpensive, abundant, chemically stable, and does not require the addition of external chemicals or produce any hazardous waste [1]. It is used in a wide variety of applications ranging from antibacterial, anti-fogging, anti-biofouling surfaces, sensors, to water and air treatment and purification by photocatalysis [1–12]. In

☆ *Disclaimer*: Although the research described in this article has been funded in part by the U.S. Environmental Protection Agency through grant/cooperative agreement (R833223) to Dionysios D. Dionysiou, it has not been subjected to the Agency's required peer and policy review and therefore does not necessarily reflect the views of the Agency and no official endorsement should be inferred.

* Corresponding author. Tel.: +1 513 556 0724; fax: +1 513 556 2599.
E-mail address: dionysios.d.dionysiou@uc.edu (D.D. Dionysiou).

0926-3373/$ – see front matter © 2010 Elsevier B.V. All rights reserved.
doi:10.1016/j.apcatb.2010.06.017

order to generate the oxidizing species (i.e., hydroxyl radicals) for photocatalytic oxidation, conventional TiO_2 requires energy below 400 nm which corresponds to a band gap of ~3.2 eV for anatase TiO_2. The possibility to extend the photoresponse capacity of TiO_2 to the visible region and be able to utilize a higher portion of the solar spectrum has become a topic of great interest among the scientific community. Metal doping of TiO_2 has yielded various results [11]. However, the use of metal doped TiO_2 for water treatment can lead to possible toxicity due to leakage of the metal ion into the finished water, diminishing its quality. Non-metal doping with elements such as nitrogen, fluorine, carbon and/or sulfur appears to be more efficient than metal doping to yield TiO_2 with high photocatalytic activity under visible light irradiation [9,10,12–16]. The photocatalytic activity under visible light has been attributed to the narrowing of the band gap, the introduction of localized intra-gap states by the dopants or the formation of surface oxygen vacancies [12,13,16].

Several studies have employed these non-metal doped TiO_2 nanoparticles for the degradation of recalcitrant organic pollutants in water [5,9,10]. The possible mobility of suspended TiO_2 nanoparticles in the environment requires an additional filtration step for the processed water and imposes a health risk due to the possible toxicity of these nanoparticles [17]. Immobilization of TiO_2 in the form of films avoids the need of filtration of nanosized TiO_2 particles of the treated effluent, an additional unit operation in the treatment train, and is a more cost-effective design for water purification. Nitrogen-doped films have been synthesized by chemical vapor deposition [18], low-energy ion implantation [19], pulsed laser deposition [20], ion-assisted electron-beam evaporation [21,22], reactive sputtering [23] and thermal nitridation [24]. The well known sol–gel method has been widely used for the preparation of nanostructured TiO_2 films. However, most of the synthesis route using sol–gel techniques involve precipitation of the non-metal doped nanoparticles [5,9,25] and cannot be employed in the preparation of TiO_2 films by dip-coating or spin-coating procedures which require stable sols. A sol–gel method can have the advantage over other techniques for both powder and film synthesis in a one-step process. In addition to doping of TiO_2 for visible light-photoactivation, the design of a well-defined TiO_2 crystal structure along with other structural characteristics (i.e., surface area, porosity, pore size distribution) plays a major role in the enhancement of light absorbance and surface interaction with micropollutants to maximize catalyst utilization. The use of self-assembled surfactants as a template material is advantageous for the formation of controlled porous TiO_2 films with high surface area, since it plays a key role in controlling the hydrolysis and condensation rates of the titanium precursor in the sol formulation [3,6,7].

In this work, a nonionic fluorosurfactant, typically employed as antistatic, anti-fogging and wetting agent [10], was used as a pore template and doping source for the synthesis of NF-TiO_2 films whose morphological, structural and electronic properties were thoroughly characterized. The application of such co-doped TiO_2 film for the remediation of water contaminated with microcystin-LR (MC-LR), the most toxic isoform of the group of microcystins, was further explored. Such technology can lead to a sustainable remediation process for cyanotoxin-contaminated water since conventional treatment methods (i.e., filtration, coagulation and sedimentation) have shown limited efficacy [1,26] and photochemical oxidation with undoped TiO_2 requires high cost UV radiation.

2. Materials and methods

The pore directing agent and fluorine source employed in the modified sol–gel solution was a nonionic fluorosurfactant (Zonyl FS-300 (FS), ~50% solids in H_2O, $R_fCH_2CH_2O(CH_2CH_2O)_xH$; $R_f = F(CF_2CF_2)_y$ where $x = 14$ and $y = 3$), purchased from Aldrich (Fluka). The fluorosurfactant was dissolved in isopropanol (i-PrOH, Fisher) and then a specific amount of acetic acid (Fisher) was added to maintain a low pH and for esterification reaction with isopropanol to produce water molecules *in situ* [6]. Before adding the titania precursor, anhydrous ethylenediamine (EDA, Fisher) was introduced in the solution as nitrogen source. Then, titanium (IV) isopropoxide (TTIP, 97%, Aldrich) was added dropwise under vigorous stirring and more acetic acid was added for peptidization. The final solution obtained was transparent, homogeneous and stable after stirring overnight at room temperature. The FS:i-PrOH:acetic acid:EDA:TTIP molar ratio employed for the preparation of the sol was *R*:275:422:46:21 where *R* is the surfactant concentration and was varied in the range from 1.0 to 5.0.

For the synthesis of NF-TiO_2 films, borosilicate glass (Micro slide, Gold Seal) was employed as substrate for the dip-coating method. The whole surface was thoroughly cleaned with MilliQ grade water followed by ethanol and drying in air. A home dip-coating apparatus with a speed controller device was used to dip in and pull out the substrate from the sol at a withdrawal rate of 12.5 ± 0.3 cm min^{-1} for a final effective surface area of 10 cm^2. After coating, the film was dried with an infrared lamp for 20 min and calcined in a multi-segment programmable furnace (Paragon HT-22-D, Thermcraft) where the temperature was increased at a ramp rate of 60 °C h^{-1} to 400 °C, maintained for 30 min and cooled down naturally. The dip-coating and calcination procedure was repeated until three layers were obtained.

As reference, TiO_2 films (3 layers total) were synthesized following the same procedure but without the addition of surfactant and ethylenediamine in the sol. A semitransparent film was obtained after calcination procedure. For comparison, P-25-containing TiO_2 films (3 layers total) were prepared with a sol–gel using Tween 20 (0.12 M) dissolved in isopropanol (5.14 M) and water (21.87 M). Then acetic acid (1.38 M) and TTIP (0.052 M) were added. Finally, P-25 TiO_2 powder (Degussa, Germany) was added in the modified sol at a concentration of 0.08 g ml^{-1}.

2.1. Characterization of the films

The viscosity of the sol with different *R* values was measured with a Brookfield rotational viscometer with No. 2 LV spindle at 50 rpm. The crystallographic structure of the synthesized TiO_2 films was determined with a X'Pert PRO (Philips) XRD diffractometer with Cu Kα (λ = 1.5406 Å) radiation. A Tristar 3000 (Micromeritics) porosimeter analyzer was employed for the determination of BET surface area, pore volume, porosity, BJH pore size and distribution of the NF-TiO_2 films. The samples were scraped from the substrate, collected as powder and purged with nitrogen gas for 2 h at 150 °C using Flow prep 060 (Micromeritics). A JEM-2010F (JEOL) high resolution-transmission electron microscope (HR-TEM) with field emission gun at 200 kV was used to obtain information on crystal size and crystal structure. The samples were dispersed in methanol (HPLC grade, Pharmco) using an ultrasonicator (2510R-DH, Bransonic) for 5 min and fixed on a carbon-coated copper grid (LC200-Cu, EMS). The film morphology was characterized with an environmental scanning electron microscope (ESEM, Philips XL 30 ESEM-FEG) at an accelerating voltage of 30 kV. A Burleigh's AFM Metris 2000 instrument was used to observe the surface roughness of the synthesized films. The elemental composition and electronic structure was determined with an X-ray photoelectron spectroscope (XPS, PerkinElmer Model 5300) with Mg Kα X-rays and vacuum pressure of 10^{-8} to 10^{-9} Torr. The binding energies were calibrated with respect to C_{1s} core level peak at 284.6 eV. To investigate the effective optical band gap of the films, the UV–vis absorption spectra were obtained using a UV–vis spec-

trophotometer (Shimadzu 2501 PC) mounted with an integrated sphere attachment (ISR1200) with $BaSO_4$ as reference standard. Micro-Raman spectra were measured in backscattering configuration on a Renishaw inVia Reflex microscope using an Ar^+ ion laser (λ = 514.5 nm) and a high power near infrared (NIR) diode laser (λ = 785 nm) as excitation sources. Additional measurements were carried out on a Jobin–Yvon triple spectrometer using the 457.9 nm Ar^+ ion laser line. The laser beam was focused onto the samples by means of a 50× objective producing a laser spot size of ~1.5 μm, while the laser power was kept at low levels (~0.1 mW) to avoid local heating of the samples. A large number of spectra were acquired from different spots for each studied sample, while the frequency shifts were calibrated by an internal Si reference. Electron paramagnetic resonance (EPR) measurements were performed using an X-band ($\nu \approx 9.42$ GHz) Bruker ER-200D spectrometer, interfaced with a personal computer and equipped with an Oxford ESR 900 cryostat, an Anritsu MF76A frequency counter and a Bruker 035M NMR gaussmeter. Continuous sample illumination was directly performed in the EPR cavity using a 360 W halogen lamp equipped with an IR water filter and a 430 nm cut-off filter for visible light illumination.

2.2. Photocatalytic experiments with MC-LR

An aqueous solution with an initial concentration of 500 $\mu g\,L^{-1}$ of MC-LR previously adjusted at pH 3.0 ± 0.1 with H_2SO_4, was used for the photocatalytic evaluation of the synthesized NF-TiO_2 films. The solution was irradiated in the visible with two 15 W fluorescent lamps (Cole–Parmer) mounted with UV block filter (UV420, Opticology) and light intensity of 7.81×10^{-5} W cm^{-2} determined with a radiant power meter (Newport Corporation). A borosilicate glass vessel reactor was sealed and cooled down with a fan to prevent evaporation. For the experiments under UV irradiation, two 15 W low-pressure mercury UV tubes (Spectronics) emitting UV radiation with a peak at 365 nm were employed. An IL 1700 radiometer with a 365 nm sensor (International Light Inc.) was used to determine the intensity and found to be 4.6×10^{-5} W cm^{-2}. The concentration of MC-LR in the samples was determined by liquid chromatography according to a method reported by Antoniou et al. [1]. All photocatalytic experiments were performed in an Advanced SterilChemgard III Class II (Baker) biological cabinet for health and safety reasons [1].

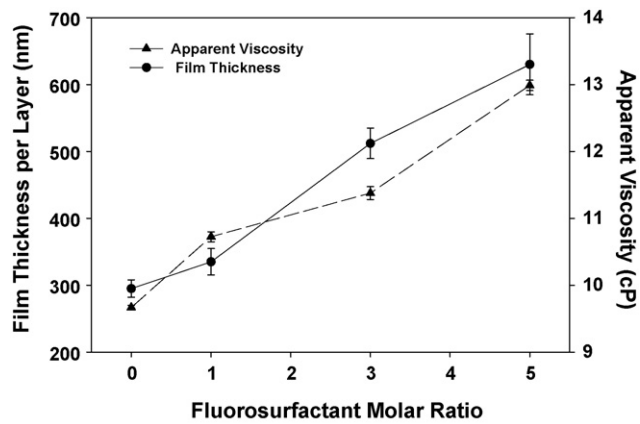

Fig. 1. Effect of fluorosurfactant loading on film thickness and apparent viscosity of the sol–gel.

3. Results and discussion

3.1. Morphology and microstructure of NF-TiO_2 films

The effect on the apparent viscosity *vs* film thickness for the different fluorosurfactant molar ratios tested can be seen in Fig. 1.

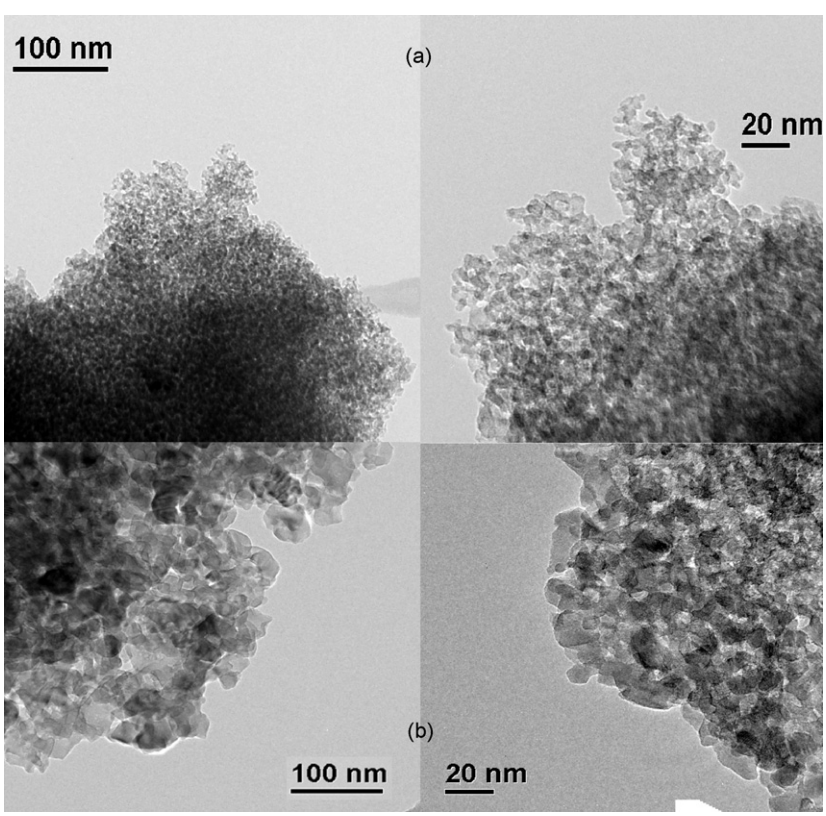

Fig. 2. HR-TEM image of (a) NF-TiO_2 with R = 5 and (b) reference TiO_2.

Table 1
Structural characteristics of NF-TiO_2 films with different fluorosurfactant ratio and reference materials.

Material	S_{BET} ($m^2\,g^{-1}$)	Pore volume ($cm^3\,g^{-1}$)	Porosity (%)[a]	Crystal phase	Crystal size (nm)[b]	$D_{(101)}$ (Å)[c]
P25 film	56.6	0.303	36.1	Anatase (75%), rutile (25%)	28.17	3.52
Reference	33.6	0.087	25.3	Anatase	12.10	3.51
$R=1$	91.4	0.137	34.9	Anatase	11.28	3.52
$R=3$	121.2	0.198	43.6	Anatase	10.65	3.51
$R=5$	136.2	0.234	47.8	Anatase	8.78	3.50

[a] Based on pore volume and 3.9 g/cm^3 of anatase density.
[b] Based on XRD using Scherrer's equation: $D = 0.9\lambda/(B \times \cos\theta)$, where $\lambda = 0.154$ nm and B = full width at half maximum (FWHM) of the highest peak.
[c] Based on Bragg's Law: $d = \lambda/(2 \times \sin\theta)$, where $\lambda = 1.54$ Å.

The film thickness was calculated based on the density of anatase phase, the porosity and weight of the film since cross-section ESEM images may cause larger error due to the high roughness of the film (see also AFM image). As expected, an increase of the fluorosurfactant ratio led to an increase in the sol viscosity and therefore an increase in film thickness. When $R=5$, the sol viscosity was 1.2 times higher and the film thickness of one dip-coating layer was 1.9 times larger than with $R=1$. This is an increase in film weight from 85 $\mu g\,cm^{-2}$ to almost twice the weight (160 $\mu g\,cm^{-2}$). Therefore, increasing the fluorosurfactant loading can increase film thickness and weight due to the increase in apparent sol viscosity. This is a promising strategy to obtain TiO_2 thicker films with high photocatalytic activity under visible light and using low concentration of surfactant and few dip-coating cycles.

A defined bicontinuous pore structure with a crystalline interconnected network can be observed from the HR-TEM images in Fig. 2. When $R=1$, the film porosity was 34.9% and increased to 47.8% when R was increased to 5. The reference film was less uniform and a more collapsed network was observed, indicating less porosity of the film (25.3%). The BET surface area also increased from 91.4 to 121.2 and 136.2 $m^2\,g^{-1}$ when the fluorosurfactant molar ratio increased from $R=1$ to 3 and 5, respectively (see Table 1). The pore size variability using a fluorosurfactant as template material was explored by measuring N_2 adsorption–desorption isotherms. As shown in Fig. 3, the pore size distribution at different fluorosurfactant ratios is similar. All of these phenomena are associated with the role of the fluorosurfactant in the sol. The fluorosurfactant acts a pore-structure-forming agent and an increase in the surfactant concentration would have an effect in the critical packing parameters [27]. As the surfactant concentration increases, so do the critical packing parameters due to a decrease in the amount of water available for the hydrophilic head groups in the sol. Overall, the packing geometry is affected (i.e., less curved geometry) as a larger critical packing parameter is obtained. An increase in the length of the hydrophobic tail will have a similar effect on this parameter. Since fluorosurfactants have a lower critical micelle concentration than carbon-based surfactants, they can self-assemble more easily [10]. Also, the concentration is relatively lower compared to carbon-based surfactant sol–gel strategies which affect significantly the packing parameter by pore coalescence and multimicellar interaction during heat treatment [7].

After calcination, XRD analysis revealed anatase crystal phase only for all the NF-TiO_2 films and control, except for P25 films where rutile phase was also confirmed (see Fig. 4). No other

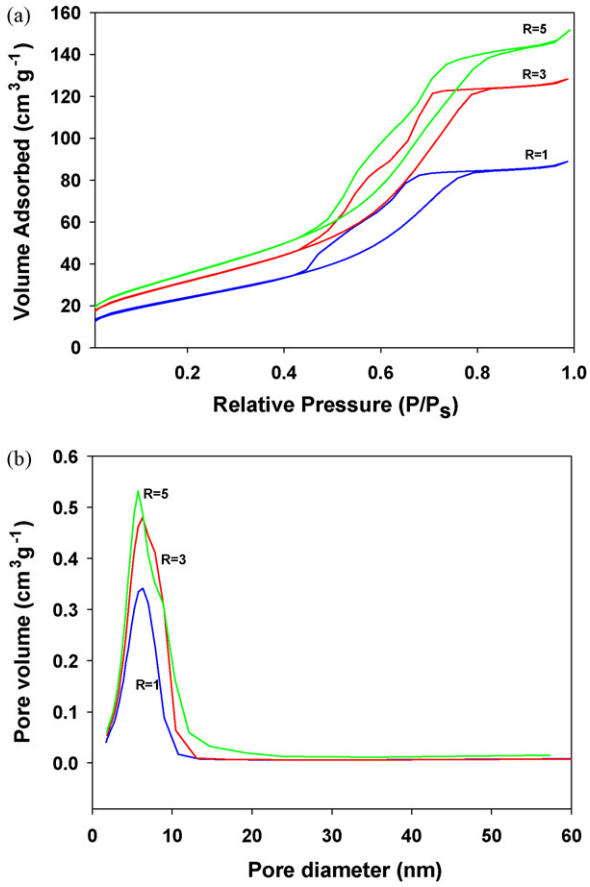

Fig. 3. (a) Nitrogen adsorption-desoprtion isotherms and (b) pore size distribution of NF-TiO_2 films with different fluorosurfactant ratio.

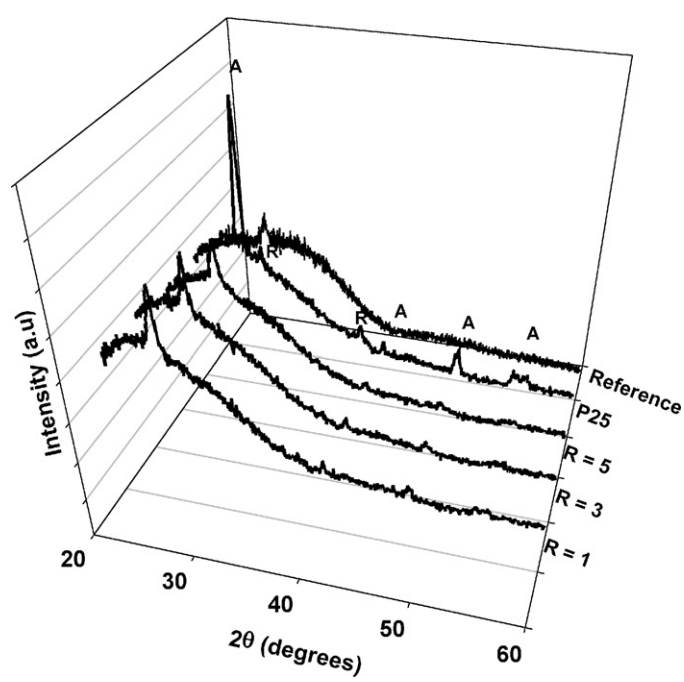

Fig. 4. XRD spectra of synthesized TiO_2 films (9 layers for reference TiO_2). Letter A corresponds to anatase phase structure and R to rutile structure.

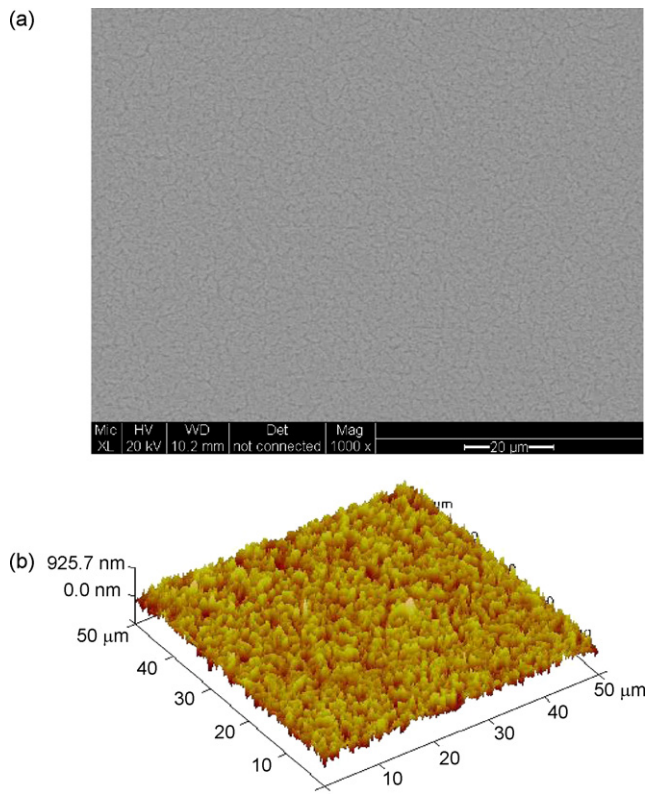

Fig. 5. ESEM and three-dimensional AFM image of NF-TiO_2 film when $R = 5$.

dopant-related crystal phases were detected during the analysis of the films. The crystalline size decreased as the surfactant ratio increased since it reduced the rate of titanium alkoxide hydrolisis and condensation of TiO_2 leading to smaller crystal size. However, the d_{space} in the (1 0 1) plane did not vary significantly leading to the conclusion that the amount of nitrogen and fluorine does not produce any significant change in the TiO_2 lattice.

The overall surface morphology of the NF-TiO_2 synthesized film was examined by ESEM and AFM and results are shown in Fig. 5. When $R = 5$, a rough but fairly uniform grain size distribution is observed after three dip-coating layers. This is in agreement with AFM analysis where the surface roughness was as high as 190 nm. An enhancement in the photocatalytic activity can be obtained with high surface roughness since rougher surface means larger surface area for the photocatalytic reactions. Moreover, light absorbance can be more effective in these rough surfaces than in smoother ones [28].

The structural characteristics and phase composition of the samples were further investigated by micro-Raman spectroscopy. Fig. 6a and b display the Raman spectra of the NF-TiO_2 sample in comparison with the reference TiO_2 sample at 514 and 785 nm, respectively. Both samples exhibit the characteristic Raman-active modes of the anatase TiO_2 phase. Anatase belongs to the tetragonal space group D_{4h}^{19} ($I4_1/amd$) leading to six Raman-active modes ($A_{1g} + 2B_{1g} + 3E_g$) [29], the most intense being the bands at 141.3 cm^{-1} (E_g), 394.4 cm^{-1} (B_{1g}), 516.1 cm^{-1} (A_{1g}, B_{1g}) and 636.7 cm^{-1} (E_g), as recently reported for bulk anatase [30]. These modes are clearly identified in the micro-Raman spectra of the two samples at both excitation wavelengths (Table 2), verifying the formation of well-crystallized anatase, in agreement with XRD results. However, comparison between NF-TiO_2 and the reference sample reveals considerable shift and broadening of the anatase Raman peaks for the co-doped sample, as directly evidenced in Fig. 6a and b. This behavior is the characteristic feature of size effects caused

Table 2
Position of the Raman modes observed in NF-TiO_2 and reference TiO_2 at 514.5 and 785 nm excitation wavelengths.

Peak position (cm^{-1})				Assignment
NF-TiO_2		Reference TiO_2		
514.5 nm	785 nm	514.5 nm	785 nm	
144.9	145.0	142.5	142.6	Anatase (E_g)
198	198	196	196	Anatase (E_g)
246	246			Brookite (A_{1g})
291	292			Brookite (B_{3g})
324	325	321.4	323.0	Anatase/brookite
365	365			Brookite (B_{2g})
399.2	399.3	395.1	395.3	Anatase (B_{1g})
460				Brookite (B_{3g}, B_{2g})
518.5	519.1	516.4	516.6	Anatase (A_{1g},B_{1g})
546				Brookite (B_{3g})
586				Brookite (B_{2g})
639.7	639.7	638.2	638.6	Anatase (E_g)
645	645			Brookite (A_{1g})

by the spatial confinement of optical phonons relaxing the $q = 0$ selection rule for Raman scattering in nanostructured materials [31]. In that case, the frequency shifts and increased width of the anatase Raman modes for the NF-TiO_2 sample point to a reduction of the anatase crystallite size, in qualitative agreement with the size variation derived from the XRD and BET measurements. However, application of the linear scaling between the Raman shift with the peak width of the lowest frequency E_g mode, frequently employed to estimate the anatase crystallite size [32–34], indicates quantitative agreement with the XRD crystalline size (8.8 nm *vs* 12.1 nm for the co-doped and reference sample, respectively), only when we allow for an excess broadening or frequency shift by about 2 cm^{-1} for the E_g mode. This implies that besides the reduction of the anatase crystalline size upon nitrogen and fluorine co-doping, deviations from stoichiometry caused by oxygen vacancies or interstitials [35,36] contribute in the variation of the anatase Raman modes.

Further analysis of the micro-Raman spectra reveals a series of weak though clearly discriminated peaks at approximately 246, 290, 325 and 365 cm^{-1} for NF-TiO_2, whereas only a broad Raman mode is observed at ~320 cm^{-1} in the same frequency range for the reference sample, as shown in Fig. 6c and d. The latter peak along with a broad Raman mode at ~796 cm^{-1}, which is also present in the reference TiO_2 sample, are frequently reported in the anatase phase and they are usually attributed to two-phonon scattering and the first overtone of the anatase B_{1g} mode at ~398 cm^{-1}, respectively [29,37,38]. On the contrary, the distinct Raman peaks in the range of 240–370 cm^{-1} are a characteristic feature of the NF-TiO_2 sample. Similar Raman peaks have been recently reported in N-doped [39] and C–N co-doped TiO_2 [40]. In that case, however, three broad peaks (320, 560 and 700 cm^{-1}) resolved at higher frequencies by spectral fitting, were assigned to the presence of Ti–N vibrations, based on the Raman scattering of non-stoichiometric titanium nitride (TiN). However, a recent Raman study of N-doped TiO_2 at variable excitation wavelengths, revealed that the intense low frequency acoustic mode of non-stoichiometric TiN at ~250 cm^{-1}, is absent, while the broad modes at higher frequencies are essentially defect-activated Raman bands that become strongly enhanced as the excitation energy increases toward the TiO_2 band gap [16].

A consistent interpretation of the weak Raman peaks for the NF-TiO_2 sample can be derived if the presence of a small fraction of the brookite TiO_2 polymorph was allowed without implicating the formation of non-stoichiometric TiN. Specifically, the weak Raman peaks at 246, 290, 325 and 365 cm^{-1} conform with the fundamental Raman modes of the orthorhombic brookite phase (space group D_{2h}^{15}) [41], whose growth has been found to be promoted,

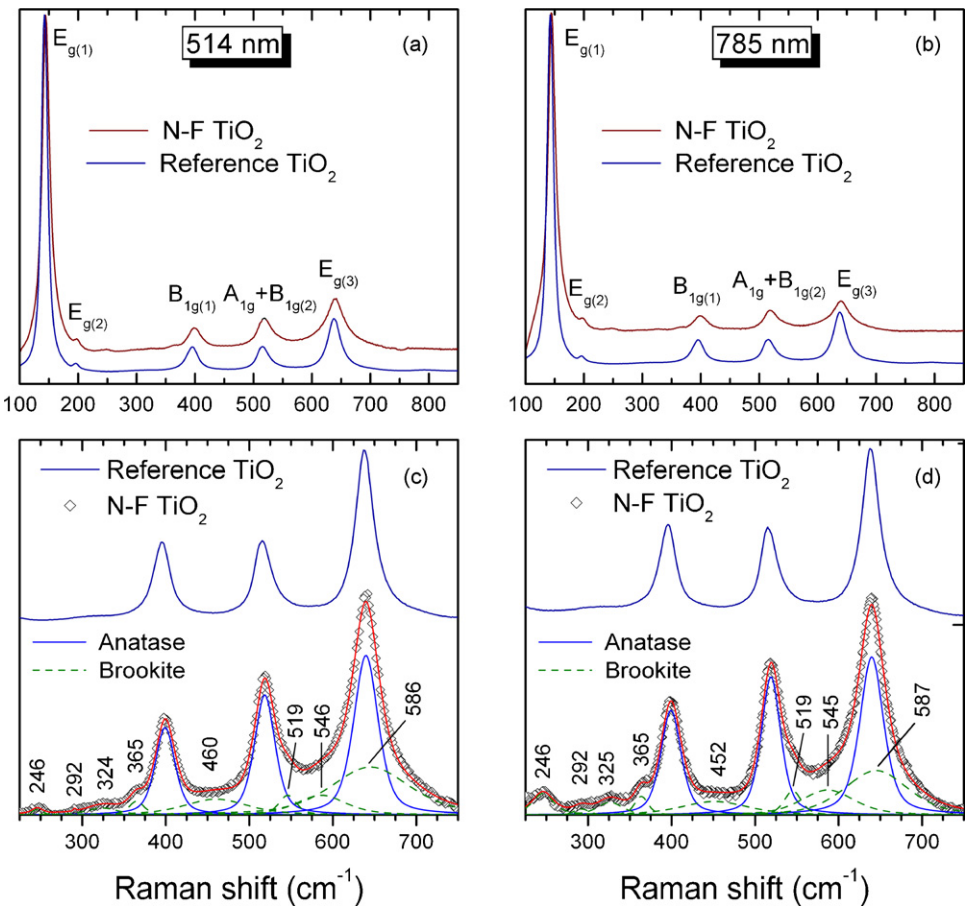

Fig. 6. Micro-Raman spectra of the NF-TiO_2 ($R = 5$) in comparison with the reference one at 514 nm (a and c) and 785 nm (b and d). The upper panels indicate the anatase Raman modes for the two samples at both excitation wavelengths. The lower panels show in detail the multi-peak fitting results (red solid line) for the Raman spectrum of NF-TiO_2 (open symbols), where the anatase and brookite peaks are depicted by blue solid and green dashed lines, respectively. (For interpretation of the references to colour in this figure legend, the reader is referred to the web version of the article.)

apart from the use of low Ti/H_2O molar ratio and high pH values during sol–gel synthesis [42], by nitrogen agents such as amines and urea [43,44]. Spectral fitting of the Raman peaks based on the contribution of both anatase as the major phase and brookite as the minor one (Table 2), accounts well for all the observed Raman bands in the NF-TiO_2 sample at both excitation wavelengths; as shown in Fig. 6c and d. Although the differentiation of possible defect-activated Raman bands from the brookite ones in the range of 380–800 cm^{-1}, where the anatase bands are dominant, cannot be conclusively determined, the lower frequency peaks at 240–370 cm^{-1} clearly identify the presence of brookite. This is further supported by the micro-Raman spectra at 457.9 nm, where no enhancement of the relative intensity of the low frequency modes could be traced with respect to the anatase Raman bands, as would be expected for the brookite phase whose energy gap lies in the UV range.

The presence of brookite/anatase heterojunctions in the NF-TiO_2 could be beneficial for its photocatalytic activity under both visible and UV irradiation, as anatase/brookite polymorphs have been recently found to markedly augment the photocatalytic efficiency [45–47], most probably through rapid interparticle electron transfer between the constituent titania nanocrystals that slow down recombination losses, similar to the highly active mixed phase titania photocatalyst Degussa P25 [48]. In addition, the favorable structural conformation of the brookite surface for water adsorption [49] could improve the photo-induced hydrophilic conversion and surface reactivity though the formation of abundant hydroxyl radicals that are important for both pollutant adsorption on the photocatalyst surface [50] and its self-cleaning ability [51].

3.2. Optical and electronic properties of NF-TiO_2 films

Tauc plots of the Kubelka–Munk function were used to obtain the indirect band gap values of the synthesized films from the absorption spectra by extrapolating the linear part of the corresponding curves in Fig. 7. Band gap values equal of 2.85 eV were found for NF-TiO_2 when $R = 5$ and 3.1 eV for P25 films. Since the reference film obtained was semitransparent, the spectrum was obtained without using the integrating sphere attached to the UV–vis spectrophotometer (data not shown) and a direct comparison cannot be made. However, the bang gap value obtained was ~3.3 eV, which is consistent with conventional TiO_2 band gap values [16,25]. The reduction of the band gap energy of NF-TiO_2 compared to the undoped films indicates a slight red shift on the absorbance towards the visible region of the spectra originated from the synergistic effect produced by co-doping TiO_2 with nitrogen and fluorine. It has been reported that the formation of localized intra-gap states above the upper level of the valence band by nitrogen doping is responsible for the new absorption band [10,16]. On the other hand, fluorine doping does not have an effect in the absorbance edge of TiO_2 but may create surface oxygen vacancies that could lead to a visible light response [13].

The nature of nitrogen and fluorine in the synthesized films was explored by XPS. The high resolution spectra of N_{1s} and F_{1s} core level of NF-TiO_2 when $R = 5$ is shown in Fig. 8. By curve fit-

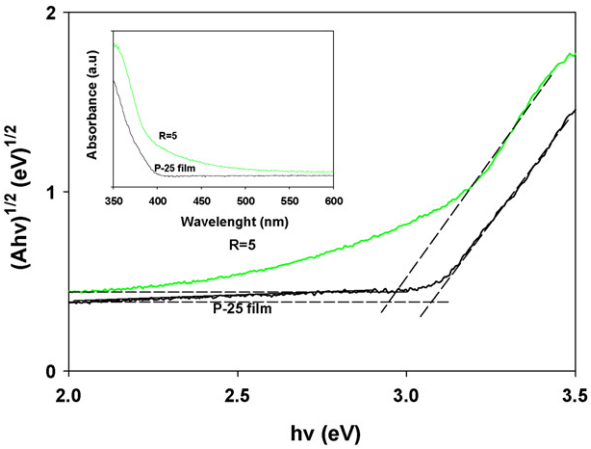

Fig. 7. Tauc plots of NF-TiO_2 with $R = 5$ compared to the P-25 film. The insert displays the UV–vis absorption spectra.

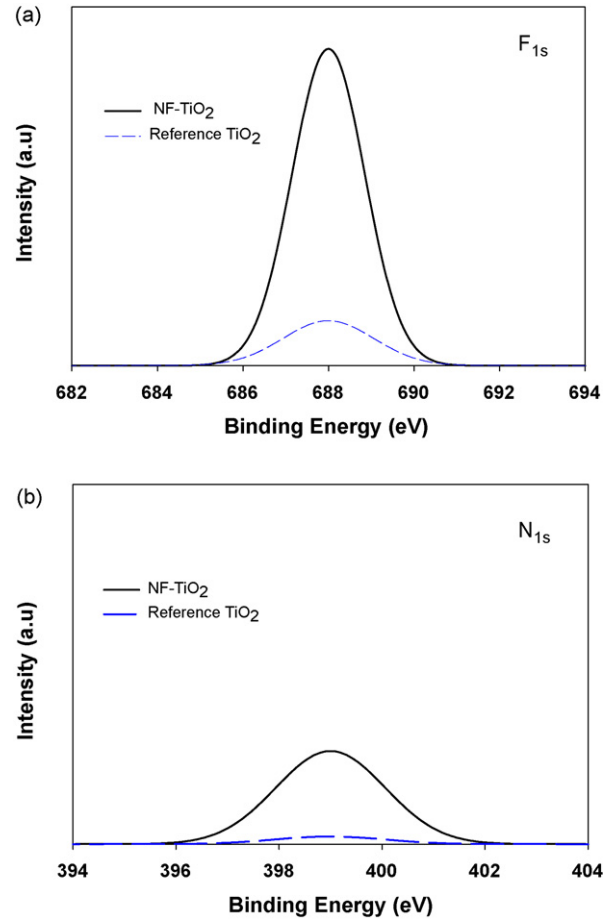

Fig. 8. High resolution XPS of (a) F_{1s} and (b) N_{1s} of NF-TiO_2 ($R = 5$) and reference TiO_2.

ting, the peak with a centered binding energy at 399.5 eV for N_{1s} indicates that nitrogen is incorporated at the interstitial site which induced the formation of localized mid-gap energy levels in the TiO_2 band gap achieving visible light-photoactivation (see also EPR analysis). This is in agreement with previous studies that employed amine compounds as their source for nitrogen doping in sol–gel routes [5,9]. The binding energy of F_{1s} was located at 688.5 eV and identified as substitutional site for fluorine in the TiO_2 lattice. F-containing compounds adsorbed on the surface can be ruled out since they have been attributed to peaks detected at 685.3 eV [13]. Substitutional fluorine inhibits the electron–hole recombination rate enhancing the photocatalytic activity by charge compensation between F^- and Ti^{4+}. It can also induce visible light photocatalytic activity by the creation of surface oxygen vacancies [10,13]. Similar binding energies were found for both nitrogen and fluorine prepared under supercritical conditions [52]. This suggests that the incorporation of both dopants favors interstitial and substitutional sites for nitrogen and fluorine, respectively. The atomic concentration of nitrogen and fluorine was 1.5% and 1.9%, respectively, at $R = 5$. For the reference sample, 0.4% for fluorine and 0.2% for nitrogen was obtained, probably from impurities of the ingredients employed and/or contaminants from air during synthesis.

The presence of localized paramagnetic species induced in the TiO_2 lattice by N–F co-doping has been investigated by EPR spectroscopy. Fig. 9 compares the EPR spectra of the NF-TiO_2 with the reference TiO_2 at 10 K and room temperature, carried out both before (dark conditions) and during visible light illumination. In the latter case, the EPR spectra are presented under continuous illumination with no UV filter that was deliberately avoided in order to enable simultaneous irradiation of the specimens by UV light, allowing both photoexcitation of the reference TiO_2 and direct comparison with the visible active NF-TiO_2 under identical illuminating conditions. An intense, slightly asymmetric EPR line at $g = 2.0030$ is observed in the dark for NF-TiO_2 at 10 K, accompanied by two weaker features at $g \sim 2.019$ and $g \sim 1.988$, characteristic of the triplet ^{14}N ($I = 1$) hyperfine structure with a coupling constant A of about 31 G (Fig. 9a). Similar EPR spectra with a weakly anisotropic, rhombic g-tensor ($g_1 = 2.005$, $g_2 = 2.004$, $g_3 = 2.003$) and a distinct triplet pattern arising from the ^{14}N hyperfine interaction with a significant splitting constant along g_3 direction ($A_3 = 32$ G), have been systematically identified in N-doped TiO_2 prepared by sol–gel and other synthetic routes [53]. Comparison with theoretical calculations suggests that the underlying paramagnetic centers are related to single N atoms incorporated in the bulk of the TiO_2 lattice, most likely at interstitial rather than substitutional sites [54], forming localized states slightly above the TiO_2 valence band that are responsible for the visible light activation of N-doped TiO_2 [55]. The presence of similar monomeric N spin species can be accordingly inferred in the case of the NF-TiO_2 sample, though the corresponding EPR spectrum is broader than that reported in N-TiO_2 [56]. This behavior may be associated with the presence of more than one N spin species with slightly different coordination environments [57,58], resulting in the inhomogeneous broadening of the EPR spectrum.

Further evidence for the role of the latter spin species in the visible light activity of the NF-TiO_2 sample is provided by the variation of the EPR spectrum under illumination, as shown in Fig. 9a. An approximate four-fold increase of the EPR intensity, derived by double integration of the resonance signal, is obtained, in good agreement with the increase of the EPR intensity of the corresponding spin species in N-TiO_2 under visible light irradiation [55].

Comparative EPR measurements on the reference sample reveal a series of very weak EPR lines before illumination at 10 K, entirely different from the N spin species observed in the NF-TiO_2 sample (Fig. 9a). An axial EPR powder spectrum can be discerned with $g_\perp = 1.998$ and $g_{||} = 1.964$ along with an asymmetric signal at $g = 1.979$ in the higher field region ($g < 2$), while several poorly resolved EPR lines are observed in the lower field region ($g > 2$) for the reference TiO_2. The former EPR signals lie within the range of g-values frequently reported for trapped electrons at Ti^{3+} sites in anatase [48,59–63], whereas the lower field signals resemble those of oxygen related paramagnetic centers in TiO_2 [64–68]. The intensity of these EPR lines is rapidly enhanced upon illumination (Fig. 9a), a characteristic feature of photo-generated oxygen radicals on anatase upon UV irradiation, comprising the contri-

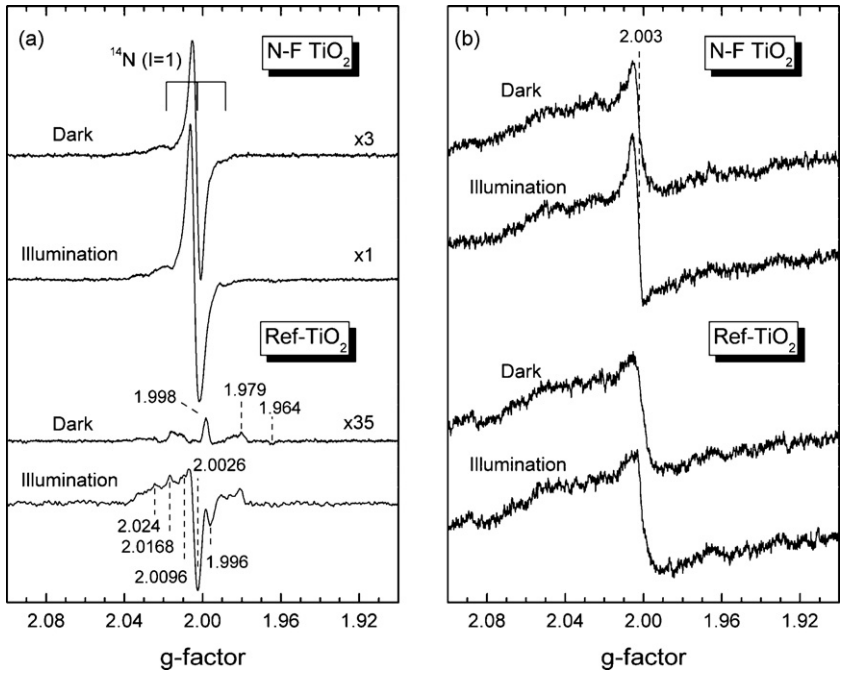

Fig. 9. EPR spectra of the NF-TiO_2 (R = 5) and reference TiO_2 samples before (dark conditions) and during visible light illumination at (a) 10 K and (b) room temperature (RT). The amplitude scale of the EPR spectra has been normalized to the same recording conditions of microwave power, modulation amplitude and receiver gain at each temperature.

bution of both surface trapped hole centers (O^-) and superoxide anions (O_2^-) in the presence of oxygen [64–68]. Control EPR experiments on the reference sample, handled in ambient conditions of moisture and oxygen, under UV irradiation and UV-filtered visible light (430–700 nm) confirmed that this behavior is related to the photoexcitation of oxygen radical species on the anatase surface by the UV part of the unfiltered illumination. These results are further corroborated by the EPR measurements carried out at room temperature, summarized in Fig. 9b. The reference sample exhibits very weak EPR lines, indicative of residual surface oxygen radicals, practically unaffected by illumination. On the other hand, an additional weak EPR line can be traced at $g \sim 2.003$ on the NF-TiO_2 sample, which intensifies upon visible light illumination, agreeing with the persistence at room temperature of the N spin species identified in the low temperature EPR spectra. This behavior is also in agreement with the long spin-relaxation time of the underlying N paramagnetic centers in N-doped TiO_2 [53].

Recent theoretical and experimental studies on F-doped TiO_2 [13,14] have shown that fluoride (F^-) ions substituting for O^{2-} induce the formation of localized Ti^{3+} centers in the bulk of anatase, which have been directly evidenced by EPR [14]. The corresponding g-values for the paramagnetic Ti^{3+} ions are close to those of the weak axial EPR spectra observed in the reference TiO_2 sample, where a small degree of unintentional doping is derived from the XPS analysis (0.4% fluorine and 0.2% nitrogen). Moreover, a combined theoretical and EPR study of NF-TiO_2 has shown that both dopants can be incorporated in the anatase lattice, creating shallow (Ti^{3+}) and deep (N) localized states in the TiO_2 band gap [69]. Most importantly, fluorine doping has been inferred to promote the incorporation of N species in TiO_2, while the energy cost for doping can be greatly reduced via an internal charge transfer mechanism from the high lying (donor) Ti^{3+} (3d) to the low lying (acceptor), singly occupied N intra-gap states. In the present work, the absence of any appreciable concentration of Ti^{3+} ions in the NF-TiO_2 EPR spectra, which are dominated by the intense EPR spectra of paramagnetic N species, indicates that F doping indeed promotes N incorporation in TiO_2. Furthermore, the abundance of N species could be rationalized by the partial charge transfer from the paramagnetic triplet configuration with two unpaired spins on the N and Ti^{3+} states to the diamagnetic singlet configuration, where the two spins pair up on the N states leading to the formation of diamagnetic N^- and Ti^{4+} ions. Such a synergistic effect is supported by the relatively weak EPR intensity of the N paramagnetic centers in NF-TiO_2 at room temperature (Fig. 9b), compared to the corresponding intense EPR spectra readily obtained for singly N-doped TiO_2 even at RT [53,58].

3.3. Visible light photocatalysis of MC-LR

Fig. 10 shows the degradation rate of MC-LR at pH 3.0 by the different synthesized NF-TiO_2 and reference films under visible light. After 180 min of reaction time, no MC-LR degradation was observed using reference TiO_2 and P-25 films. All NF-TiO_2 samples showed photocatalytic activity with highest MC-LR degradation rate obtained when the fluorosurfactant molar ratio was 5 (3.95×10^{-5} μM min^{-1}). The photocatalytic activity of these films was due to the effective doping with nitrogen and fluorine and their synergistic effects towards visible light photoresponse. The improvement in the structural properties (i.e., BET surface area, porosity, pore volume, film thickness) of the synthesized films when increasing the fluorosurfactant loading in the sol is also responsible of the enhancement in the photocatalytic degradation rate of MC-LR.

In order to rule out the possibility that some irreversible change of the catalyst occurred during the irradiation experiments and to investigate the stability of the films, the performance of the catalyst was explored during reuse application. It was interesting to find that, as shown in Fig. 10a, no irreversible changes of the catalyst occurred after 180 min of reaction time, since rather stable degradation rates were obtained when reutilizing the catalyst after 3 cycles under visible light. This indicates that the films possess high mechanical stability since the loss of catalyst was negligible during washing and reusing and can be used repetitively for extended

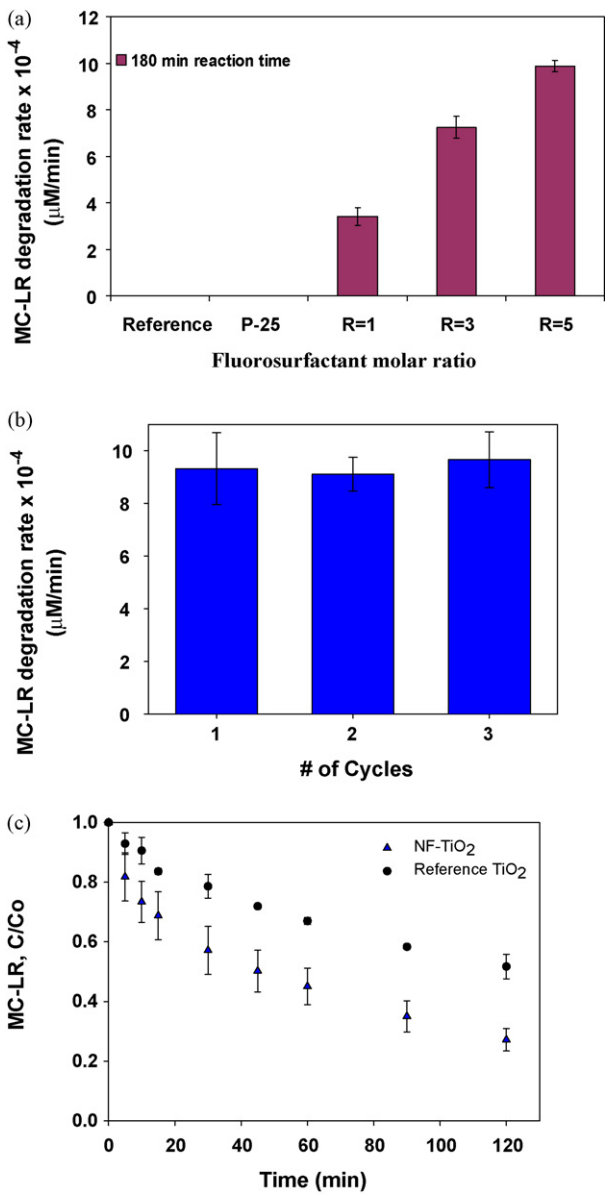

Fig. 10. (a) MC-LR degradation rate at pH 3.0 with synthesized films under visible light ($\lambda > 420$ nm) after 180 min of reaction time (b) effect of reuse of NF-TiO_2 film and (c) MC-LR degradation under UV illumination with NF-TiO_2 ($R = 5$) and reference TiO_2.

periods of time. This ensures that most of the nitrogen and fluorine dopants are incorporated into the TiO_2 lattice and therefore leaching or transformation during the photocatalytic process is not likely to occur at least under the conditions employed in this study. Furthermore, large amounts of nitrogen and fluorine species adsorbed at the surface of the catalyst inhibit the photocatalytic reactions by covering the TiO_2 surface and also capture the holes induced by photoexcitation of the catalyst [52], which was not observed with these films after 3 cycles.

Under UV illumination, both reference TiO_2 and NF-TiO_2 films effectively degraded MC-LR at pH 3.0 (see Fig. 10c). However, the photocatalytic activity for the degradation of the cyanotoxin was higher with NF-TiO_2 compared to reference TiO_2. This is due to several factors that played an important role including a better UV response of NF-TiO_2, enhanced structural properties (i.e., high surface area, small crystallite size, and high porosity), and the presence of brookite/anatase heterojunctions. As mentioned before, these polymorphs may reduce recombination rates by a rapid interparticle electron transfer between the nanocrystals and increase the photocatalytic activity of the catalyst.

4. Conclusions

A modified sol–gel method was applied to synthesize active visible light-activated NF-TiO_2 films with controlled nanostructure. Relatively small amount of fluorosurfactant and a small number of dip-coating cycles were employed to obtain visible light-activated NF-TiO_2 films. Besides the co-doping of nitrogen and fluorine for visible light photoresponse of the catalyst, the increase of fluorosurfactant in the sol leads to improvement in the physicochemical (i.e., surface area, crystal size, porosity) and optical properties compared to reference materials. According to micro-Raman analysis, this synthesis route results in the formation of nanocrystalline anatase as the major TiO_2 phase together with a small fraction of brookite, which could promote the photocatalytic activity through the formation of anatase/brookite heterojunctions. EPR measurements revealed the presence of paramagnetic N spin species in the co-doped TiO_2, whose concentration is markedly enhanced under visible light irradiation. The dominance of these paramagnetic species underlying the visible light photo-activity of NF-TiO_2 indicates that fluorine facilitates nitrogen incorporation in TiO_2, while the absence of reduced Ti^{3+} ions anticipated through single F-doping supports the presence of partial charge transfer and synergistic effects between the F and N dopants. The synthesized films were active and mechanically stable in the degradation of MC-LR under visible and UV light under acidic conditions. We believe that this study on NF-TiO_2 films sets a firm basis for the development and design of effective flow-through solar-based photocatalytic reactors for environmental applications, such as the treatment of water contaminated with cyanotoxins.

Acknowledgements

This work was funded in part by the U.S. Environmental Protection Agency (R833223), the National Science Foundation through a CAREER award (BES-0448117) to Dionysios D. Dionysiou and the European Commission (Clean Water—Grant Agreement number 227017). Clean Water is a Collaborative Project co-funded by the Research DG of the European Commission within the joint RTD activities of the Environment and NMP Thematic Priorities/FP7. Dr. N. Ioannidis (NCSR Demokritos) is acknowledged for his expert assistance in the light-dependent EPR measurements.

References

[1] M.G. Antoniou, J.A. Shoemaker, A.A. de la Cruz, D.D. Dionysiou, Toxicon 51 (2008) 1103–1118.
[2] Y. Chen, E. Stathatos, D.D. Dionysiou, Surf. Coat. Technol. 202 (2008) 1944–1950.
[3] Y. Chen, D.D. Dionysiou, Appl. Catal. B 80 (2008) 147–155.
[4] H. Choi, E. Stathatos, D.D. Dionysiou, Desalination 202 (2007) 199–206.
[5] Y. Liu, J. Li, X. Qiu, C. Burda, J. Photochem. Photobiol. A 190 (2007) 94–100.
[6] H. Choi, E. Stathatos, D.D. Dionysiou, Thin Solids Films 510 (2006) 107–114.
[7] H. Choi, A.C. Sofranko, D.D. Dionysiou, Adv. Funct. Mater. 16 (2006) 1067–1074.
[8] S.K. Lunsford, H. Choi, J. Stinson, A. Yeary, D.D. Dionysiou, Talanta 73 (2007) 172–177.
[9] H. Choi, M.G. Antoniou, M. Pelaez, A.A. de la Cruz, J.A. Shoemaker, D.D. Dionysiou, Environ. Sci. Technol. 41 (2007) 7530–7535.
[10] M. Pelaez, A.A. de la Cruz, E. Stathatos, P. Falaras, D.D. Dionysiou, Catal. Today 144 (2009) 19–25.
[11] F. Han, V.S.R. Kambala, M. Srinivasan, D. Rajarathnam, R. Naidu, Appl. Catal. B 359 (2009) 25–40.
[12] R. Asahi, T. Morikawa, K. Aoki, Y. Taga, Science 293 (2001) 269–271.
[13] D. Li, N. Ohashi, S. Hishita, T. Kolodiazhnyi, H. Haneda, J. Solid State Chem. 178 (2005) 3293–3302.
[14] A.M. Czoska, S. Livraghi, M. Chiesa, E. Giamello, S. Agnoli, G. Granozzi, E. Finazzi, C. Di Valentin, G. Pacchioni, J. Phys. Chem. C 112 (2008) 8951.
[15] P. Periyat, S.C. Pillai, D.E. McCormack, J. Colreavy, S.J. Hinder, J. Phys. Chem. C 112 (2008) 7644–7652.

[16] A.I. Kontos, A.G. Kontos, Y.S. Raptis, P. Falaras, Phys. Stat. Sol. (RRL) 2 (2008) 83–85.
[17] M.R. Wiesner, G.V. Lowry, P. Alvarez, D.D. Dionysiou, P. Biswas, Environ. Sci. Technol. 40 (2006) 4336–4345.
[18] I. Justicia, P. Ordejon, G. Canto, J.L. Mozos, J. Fraxedas, G.A. Battiston, R. Gerbasi, A. Figueras, Adv. Mater. 14 (2002) 1402.
[19] H. Shen, L. Mi, P. Xu, W. Shen, P.N. Wang, Appl. Surf. Sci. 253 (2007) 7024.
[20] Y. Suda, H. Kawasaki, T. Ueda, T. Ohshima, Thin Solid Films 453–454 (2004) 162.
[21] T.-S. Yang, M.-C. Yang, C.-B. Shiu, W.-K. Chang, M.-S. Wong, Appl. Surf. Sci. 252 (2006) 3729.
[22] M.-S. Wong, W.-C. Chu, D.-S. Sun, H.-S. Huang, J.-H. Chen, P.-J. Tsai, N.-T. Lin, M.-S. Yu, S.-F. Hsu, S.-L. Wang, H.-H. Chang, Appl. Environ. Microb. 72 (2006) 6111.
[23] S.-Z. Chen, P.-Y. Zhang, D.-M. Zhuang, W.-P. Zhu, Catal. Commun. 5 (2004) 677.
[24] E. Martínez-Ferrero, Y. Sakatani, C. Boissière, D. Grosso, A. Fuertes, J. Fraxedas, C. Sanchez, Adv. Funct. Mater. 17 (2007) 3348–3354.
[25] M. Sathish, B. Viswanathan, R.P. Viswanath, C.S. Gopinath, Chem. Mater. 17 (2005) 6349–6353.
[26] W. Schmidt, H. Willmitzer, K. Bornmann, J. Pietsch, Environ. Toxicol. 17 (2002) 375–385.
[27] Z. Zhang, Z.-L. Wang, J. Liu, S. Chen, G.-Y. Liu, Self-Assembled Nanostructures, Kluwer Academic/Plenum Publishers, New York, 2003.
[28] A. Provata, P. Falaras, A. Xagas, Chem. Phys. Lett. 297 (1998) 484–490.
[29] T. Ohsaka, F. Izumi, Y. Fujiki, J. Raman Spectrosc. 7 (1978) 321–324.
[30] G.R. Hearne, J. Zhao, A.M. Dawe, V. Pischedda, M. Maaza, M.K. Niewoudt, P. Kibasomba, O. Nemraoui, J.D. Comins, M. Witcomb, J. Phys. Rev. B 70 (2004) 134102.
[31] H. Richter, Z.P. Wang, L. Ley, Solid State Commun. 39 (1981) 625–629.
[32] S. Kelly, F.H. Pollak, M. Tomkiewicz, J. Phys. Chem. B 101 (1997) 2730–2734.
[33] V. Swamy, A. Kuznetsov, L.S. Dubrovinsky, R.A. Caruso, D.G. Shchukin, B.C. Muddle, Phys. Rev. B 71 (2005) 184302.
[34] V. Likodimos, T. Stergiopoulos, P. Falaras, J. Kunze, P. Schmuki, J. Phys. Chem. C 112 (2008) 12687–12696.
[35] C. Parker, R.W. Siegel, Appl. Phys. Lett. 57 (1990) 943–945.
[36] A. Li Bassi, D. Cattaneo, V. Russo, C.E. Bottani, E. Barborini, T. Mazza, P. Piseri, P. Milani, F.O. Ernst, K. Wegner, S.E. Pratsinis, J. Appl. Phys. 98 (2005) 074305.
[37] U. Balachandran, N.G. Eror, J. Solid State Chem. 42 (1982) 276–282.
[38] Y.H. Zhang, C.K. Chan, J.F. Porter, W. Guo, J. Mater. Res. 13 (1998) 2602–2609.
[39] Y. Cong, J. Zhang, F. Chen, M. Anpo, J. Phys. Chem. C 111 (2007) 6976–6982.
[40] X.X. Yang, C.D. Cao, L. Erickson, K. Hohn, R. Maghirang, K. Klabunde, J. Catal. 260 (2008) 128–133.
[41] G.A. Tompsett, G.A. Bowmaker, R.P. Cooney, J.B. Metson, K.A. Rogers, J.M. Seakins, J. Raman Spectrosc. 26 (1995) 57–62.
[42] S.L. Isley, R.L. Penn, J. Phys. Chem. B 110 (2006) 15134–15139.
[43] Y. Djaoued, R. Brüning, D. Bersani, P.P. Lottici, S. Badilescu, Mater. Lett. 58 (2004) 2618–2622.
[44] T. López-Luke, A. Wolcott, L.-P. Xu, S. Chen, Z. Wen, J. Li, E. de la Rosa, J.Z. Zhang, J. Phys. Chem. C 112 (2008) 1282–1292.
[45] G.H. Tian, H.G. Fu, L.Q. Jing, B.F. Xin, K. Pan, J. Phys. Chem. C 112 (2008) 3083–3089.
[46] G.S. Shao, X.J. Zhang, Z.Y. Yuan, Appl. Catal. B 82 (2008) 208–218.
[47] J.G. Yu, L.J. Zhang, B. Cheng, Y.R. Su, J. Phys. Chem. C 111 (2007) 10582–10589.
[48] D.C. Hurum, A.G. Agrios, K.A. Gray, T. Rajh, M.C. Thurnauer, J. Phys. Chem. B 107 (2003) 4545–4549.
[49] W.-K. Li, X.-Q. Gong, G. Lu, A. Selloni, J. Phys. Chem. C 112 (2008) 6594–6596.
[50] S. Ardizzone, C.L. Bianchi, G. Cappelletti, S. Gialanella, C. Pirola, V. Ragaini, J. Phys. Chem. C 111 (2007) 13222.
[51] T. Shibata, H. Irie, M. Ohmori, A. Nakajima, T. Watanabe, K. Hashimoto, Phys. Chem. Chem. Phys. 6 (2004) 1359.
[52] Y. Huo, Y. Jin, J. Zhu, H. Li, Appl. Catal. B 89 (2009) 543–550.
[53] S. Livraghi, A. Votta, M.C. Paganini, E. Giamello, Chem. Commun. 4 (2005) 498–500.
[54] S. Livraghi, M.R. Chierotti, E. Giamello, G. Magnacca, M.C. Paganini, G. Cappelletti, C.L. Bianchi, J. Phys. Chem. C 112 (2008) 17244–17252.
[55] S. Livraghi, M.C. Paganini, E. Giamello, A. Selloni, C. Di Valentin, G. Pacchioni, J. Am. Chem. Soc. 128 (2006) 15666–15671.
[56] C. Di Valentin, E. Finazzi, G. Pacchioni, A. Selloni, S. Livraghi, M.C. Paganini, E. Giamello, J. Chem. Phys. 339 (2007) 44–56.
[57] C. Di Valentin, G. Pacchioni, A. Selloni, S. Livraghi, E. Giamello, J. Phys. Chem. B 109 (2005) 11414–11419.
[58] E.A. Reyes-Garcia, Y. Sun, K. Reyes-Gil, D. Reftery, J. Phys. Chem. C 111 (2007) 2738–2748.
[59] R.F. Howe, M. Grätzel, J. Phys. Chem. 91 (1987) 3906–3909.
[60] Y. Nakaoka, Y. Nosaka, J. Photochem. Photobiol. A 110 (1997) 299–305.
[61] T. Berger, M. Sterrer, O. Diwald, E. Knözinger, D. Panayotov, T.L. Thompson, J.T. Yates, J. Phys. Chem. B 109 (2005) 6061–6068.
[62] C.P. Kumar, N.O. Gopal, T.C. Wang, M.S. Wong, S.C. Ke, J. Phys. Chem. B 110 (2006) 5223–5229.
[63] G.H. Li, N.M. Dimitrijevic, L. Chen, J.M. Nichols, T. Rajh, K.A. Gray, J. Am. Chem. Soc. 130 (2008) 5402–5403.
[64] O.I. Micic, Y.N. Zhang, K.R. Cromack, A.D. Trifunac, M.C. Thurnauer, J. Phys. Chem. 97 (1993) 7277–7283.
[65] J.M. Coronado, A.J. Maira, C.J. Conesa, K.L. Yeung, V. Augugliaro, J. Soria, Langmuir 17 (2001) 5368–5374.
[66] E. Carter, A.F. Carley, D.M. Murphy, J. Phys. Chem. C 111 (2007) 10630–10638.
[67] J.M. Coronado, J. Soria, Catal. Today 123 (2007) 37–41.
[68] R. Scotti, I.R. Bellobono, C. Canevali, C. Cannas, M. Catti, M. D'Arienzo, A. Musinu, S. Polizzi, M. Sommariva, A. Testino, F. Morazzoni, Chem. Mater. 20 (2008) 4051–4061.
[69] C. Di Valentin, E. Finazzi, G. Pacchioni, A. Selloni, S. Livraghi, A.M. Czoska, M.C. Paganini, E. Giamello, Chem. Mater. 20 (2008) 3706–3714.